APPLIED SCIENCES AND ENGINEERING

# Amorphous anion-rich titanium polysulfides for aluminum-ion batteries

Zejing Lin[1,2†], Minglei Mao[1†], Chenxing Yang[3†], Yuxin Tong[1], Qinghao Li[1,4], Jinming Yue[1], Gaojing Yang[1], Qinghua Zhang[1], Liang Hong[5], Xiqian Yu[1], Lin Gu[1], Yong-Sheng Hu[1], Hong Li[1], Xuejie Huang[1], Liumin Suo[1,2,6]*, Liquan Chen[1]



**The strong electrostatic interaction between $Al^{3+}$ and close-packed crystalline structures, and the single-electron transfer ability of traditional cationic redox cathodes, pose challenged for the development of high-performance rechargeable aluminum batteries. Here, to break the confinement of fixed lattice spacing on the diffusion and storage of Al-ion, we developed a previously unexplored family of amorphous anion-rich titanium polysulfides (a-$TiS_x$, $x = 2$, 3, and 4) (AATPs) with a high concentration of defects and a large number of anionic redox centers. The AATP cathodes, especially a-$TiS_4$, achieved a high reversible capacity of 206 mAh/g with a long duration of 1000 cycles. Further, the spectroscopy and molecular dynamics simulations revealed that sulfur anions in the AATP cathodes act as the main redox centers to reach local electroneutrality. Simultaneously, titanium cations serve as the supporting frameworks, undergoing the evolution of coordination numbers in the local structure.**

## INTRODUCTION

Accessing electrochemical systems with high energy density and good safety remains a major challenge for future large-scale energy storage. The desire to move toward a high-performance rechargeable aluminum battery (RAB) that uses trivalent $Al^{3+}$ as a charge carrier is driven by the high capacity (8046 mAh/$cm^3$), inherent safety, low cost, and abundance of Al (*1*–*3*). Great efforts have been made to seek appropriate host materials from crystalline transition metal sulfides, transition metal oxides, Prussian blue analogs, etc. (*4*–*6*). However, the development of RABs is severely hindered by the low capacity and poor reversibility of most crystalline intercalation materials used in traditional monovalent intercalation chemistry ($Li^+$ and $Na^+$) (*7*–*9*). The main reason is the strong electrostatic interaction between close-packed crystalline lattices and high–charge density $Al^{3+}$ (*10*). As shown in Fig. 1A, the intercalation reaction in crystalline materials mainly depends on the number of storage sites, solid-state ionic diffusion, and structural stability (*11*). When $Al^{3+}$ is intercalated into a fixed lattice, the surrounding electrostatic field markedly changes to attain a neutral state, resulting in sluggish diffusion kinetics of $Al^{3+}$ ions and poor reversibility (*12*, *13*). The single-electron transfer of traditional cationic redox chemistry also delays the local charge compensation process, leading to a high reaction barrier and large polarization. Furthermore, upon massive electron injection, unstable lattice distortions and irreversible structural collapse often occur, reducing the storage sites and accelerating the potential failure (*14*, *15*). Therefore, the designs for the $Al^{3+}$ host should focus on an open and unrestricted structure, and special attention should be paid to the local chemical environment and the electron-compensation ability of the active sites, as well as the short ion diffusion paths.

Amorphization (Fig. 1B) has been proven to effectively break the confinement of ordered structures and generate high concentrations of defects (vacancies and void spaces) as active sites (*16*–*20*), such as hard carbon (*21*, *22*). The formed open channels and the isotropic property are beneficial to promote solid-state ion diffusion (*23*). The large specific surface area and random short-range ordered clusters could also improve the reaction activity and reduce the marked local volume change caused by guest-ion intercalation (*24*). However, merely increasing the ion-storage sites is not sufficient to increase the capacity. An adequate number of electrons are also required to attain local neutrality during cycling (*25*). It is equally important to improve the local electron-transfer ability of active sites to quickly achieve charge balance, especially for the storage of high–charge density multivalent ions. Compared to the classical single electron–transferred cationic redox reaction, anionic redox chemistry has recently been used to regulate multiple electrons transfer from the anion centers to achieve higher capacity (*26*–*28*). Thus, building a scattered local anion-rich structure to increase anionic redox centers, as shown in Fig. 1C, may enhance the multi-electron transfer efficiency and improve capacity. It has been reported that the ratio of sulfur anions in crystalline $TiS_2$, $MoS_2$, and $NbS_2$ can be further increased to three to five at an amorphous state via soft chemical or high-energy mechanical methods (*29*–*33*). Besides, the sulfur-based anionic frameworks have been proven to enhance the mobility of Al ions owing to the low electronegativity of sulfur anions (*7*, *13*, *34*, *35*).

Here, we propose a new strategy combining amorphization and anion enrichment to explore high-capacity Al-ion cathodes, which break the confinement of fixed lattice spacing, introduce a large concentration of defects, and increase the number of anionic redox centers. A series of amorphous anion-rich titanium polysulfides (AATPs) were investigated as cathodes in RABs with an $AlCl_3$–1-ethyl-3-methyl-imidazolium chloride ([EMIm]Cl) ionic liquid electrolyte and a metallic Al anode. Compared with crystalline materials, both amorphization and sulfur enrichment strategies could

[1]Beijing Advanced Innovation Center for Materials Genome Engineering, Key Laboratory for Renewable Energy, Beijing Key Laboratory for New Energy Materials and Devices, Institute of Physics, Chinese Academy of Sciences, Beijing 100190, China. [2]Center of Materials Science and Optoelectronics Engineering, University of Chinese Academy of Sciences, Beijing 100049, China. [3]School of Materials Science and Engineering and Institute of Natural Sciences, Shanghai Jiao Tong University, Shanghai 200240, China. [4]College of Physics, Qingdao University, Qingdao, Shandong 266071, China. [5]School of Physics and Astronomy and Institute of Natural Sciences, Shanghai Jiao Tong University, Shanghai 200240, China. [6]Yangtze River Delta Physics Research Center Co. Ltd., Liyang, Jiangsu 213300, China.
*Corresponding author. Email: suoliumin@iphy.ac.cn
†These authors contributed equally to this work.

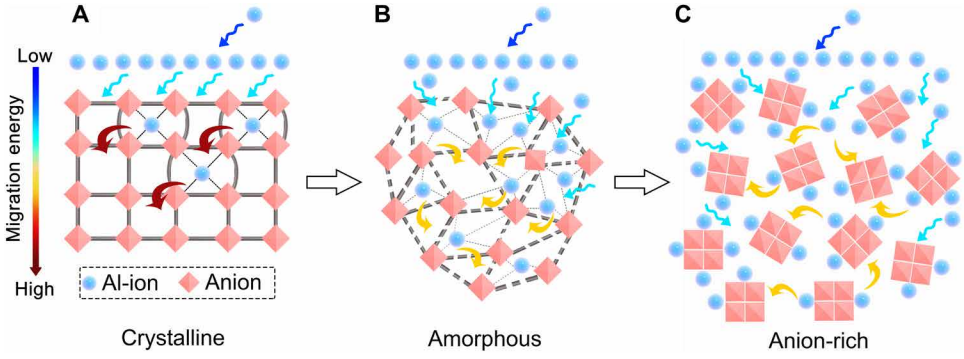


**Fig. 1. Design strategy for an amorphous anion-rich structure for Al-ion hosts.** Al-ion storage and diffusion process in (**A**) traditional crystalline materials, (**B**) amorphous materials, and (**C**) amorphous anion-rich materials.

notably improve the electrochemical performance. Among the AATPs, amorphous sulfur-rich $TiS_4$ is more prominent. Experimental and theoretical investigations further revealed that the $TiS_4$ cathode mainly underwent an anionic redox reaction and achieved local multielectron transfer. We believe that such an amorphous and anion-rich strategy can provide more possibilities for high-energy multivalent-ion batteries.

## RESULTS

### Synthesis and characterization of AATPs

The AATPs were synthesized using a facile top-down high-energy ball-milling method (Fig. 2A). With the impact, compression, friction, and shear forces from the balls and tank wall, raw crystalline particles were refined continuously and deformed to form a metastable state containing a large number of defects and dislocations with continuous breaking and recombination to form new materials during the milling process (*36*, *37*). After 48 hours of ball milling, a typical long-range ordered lattice fringe of raw crystalline $TiS_2$ (c-$TiS_2$) completely disappears and is replaced by an amorphous state with a diameter of 50 to 200 nm (Fig. 2A and fig. S1). The Ti and S elements are uniformly distributed in amorphous $TiS_3$ and $TiS_4$ (a-$TiS_3$ and a-$TiS_4$) with atomic ratios of about 1:3 and 1:4, respectively (figs. S2 and S3). The nitrogen adsorption-desorption isotherms indicate that a-$TiS_4$ has a higher surface area (16.5 $m^2$/g) than c-$TiS_2$ (7.8 $m^2$/g) (fig. S4).

In addition, the structural information of AATPs was investigated. Ex situ x-ray diffraction (XRD) patterns of the c-$TiS_2$ + S mixture were monitored during the ball-milling process (Fig. 2B). With an increase in the reaction time, the typical characteristic peaks of c-$TiS_2$ and $S_8$ constantly weakened until they completely disappeared after 48 hours, indicating the formation of a-$TiS_x$, $x = 2$, 3, and 4 (fig. S5). Differential scanning calorimetry (DSC) curves (Fig. 2C) also indicate that the endothermic peaks at 118°C and 280°C (corresponding to the melting and sublimation of sulfur, respectively) disappear in a-$TiS_3$ and a-$TiS_4$, illustrating the formation of chemical bonds between additional sulfur and titanium sulfide after milling rather than mere amorphization and mixing. Moreover, a-$TiS_4$ also exhibits higher weight loss than the crystalline c-$TiS_2$ + 2S mixture, as shown in the thermogravimetric (TG) curves (fig. S6), revealing the weak interaction of the new Ti-S bond after amorphization. Raman spectra (fig. S7) further confirm the formation of new chemical bonds, where the raw peaks ascribed to sulfur (221 and 473 $cm^{-1}$) and c-$TiS_2$ (333 $cm^{-1}$) disappear, and the new broad peaks appear at approximately 400 and 420 $cm^{-1}$ in a-$TiS_3$ and a-$TiS_4$, respectively (*38*, *39*).

The chemical states of the sulfur anions and titanium cations of AATPs were further analyzed via x-ray photoelectron spectroscopy (XPS) and x-ray absorption near-edge structure (XANES) measurements. c-$TiS_2$ displays one pair of peaks at 161.2 and 162.4 eV (Fig. 2D), assigned to the $S^{2-}$ $2p_{3/2}$ and $S^{2-}$ $2p_{1/2}$, respectively (*40*, *41*). As the sulfur ratio gradually increased to 4, these prominent peaks gradually shift to higher binding energy at 162.7 and 163.9 eV, corresponding to the $S_2^{2-}$ $2p_{3/2}$ and $S_2^{2-}$ $2p_{1/2}$, respectively (*42*). Typical double peaks of elemental sulfur at 164.1 and 165.3 eV are not observed in the sulfur-rich $TiS_3$ and $TiS_4$, further verifying the formation of chemical bonds between sulfur and titanium. XANES was conducted to further investigate the oxidation state and site symmetry of Ti in representative crystalline, amorphous, and sulfur-rich materials (Fig. 2E). The Ti *K*-edge XANES spectra of c-$TiS_2$ consist of a strong absorption peak at approximately 4978.0 eV and a relatively weak pre-edge peak at approximately 4969.5 eV. The main absorption peak is attributed to the transition of Ti 1s electrons to unoccupied 4p orbitals, and the pre-edge peak is ascribed to the transition of 1s to the 3d orbitals (*43*). The sharp decrease in intensity of the main peak further confirms the amorphous state of local structure in a-$TiS_x$ as the disordered distribution contributed to the destructive interference in multiple scattering, resulting in its lower amplitude (*44*). After amorphization, no apparent change in the adsorption edge position is observed, demonstrating that $Ti^{4+}$ is retained. Meanwhile, the pre-edge peak slightly shifts to higher energy with the decrease in its intensity, revealing an increase in the coordination number and a decrease in the symmetry of Ti in the local structure (*45*).

### Electrochemical performance of AATP/Al pouch cells

The electrochemical performance of AATP/Al pouch cells was tested to investigate the Al-ion storage in amorphous materials. The electrical conductivity of the samples was measured using a four-pin probe method (Fig. 3A and table S1). It gradually decreased from $5.9 \times 10^{-1}$ S/cm for a-$TiS_2$ to $1.3 \times 10^{-5}$ S/cm for a-$TiS_4$. To guarantee sufficient electronic conductivity of the electrode, 20 weight % (wt %) Ketjen black (KB) was added in the a-$TiS_4$/KB electrode to achieve a high electronic conductivity of $9.1 \times 10^{-2}$ S/cm. Figure 3B compares the typical discharge-charge curves of c-$TiS_2$ before and after amorphization at 0.05 A/g and 25°C. The a-$TiS_2$ exhibits a reversible capacity of 48 mAh/g, more than twice that of c-$TiS_2$

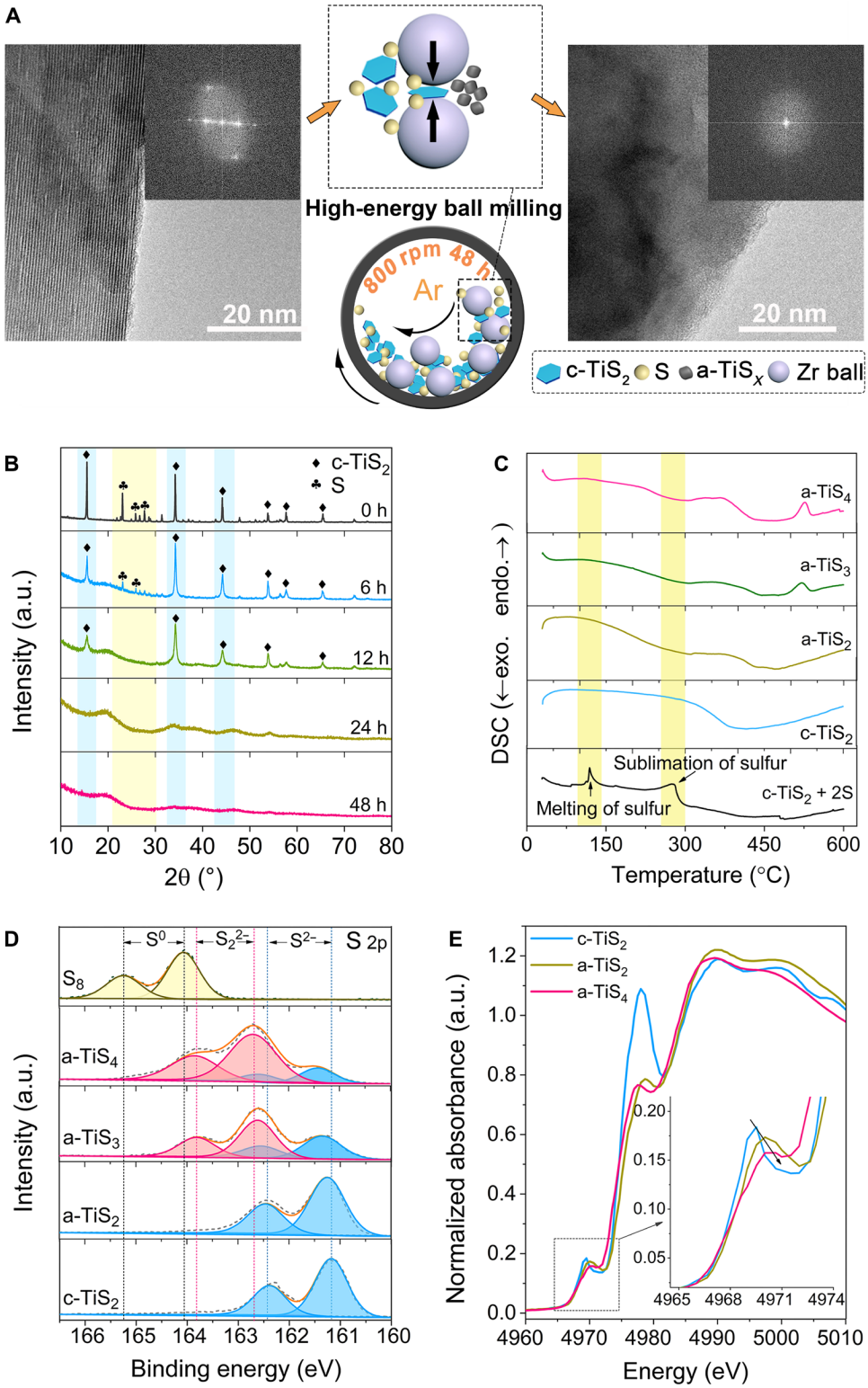


**Fig. 2. Synthesis and spectroscopic characterization of AATPs.** (**A**) Schematic of AATP synthesis process and corresponding high-resolution (HR)–TEM images of c-$TiS_2$ and a-$TiS_4$. (**B**) Ex situ XRD patterns at different milling hours, (**C**) DSC curves, (**D**) XPS S 2p spectra, and (**E**) Ti *K*-edge XANES spectra of c-$TiS_2$, a-$TiS_2$, and a-$TiS_4$. a.u., arbitrary units.

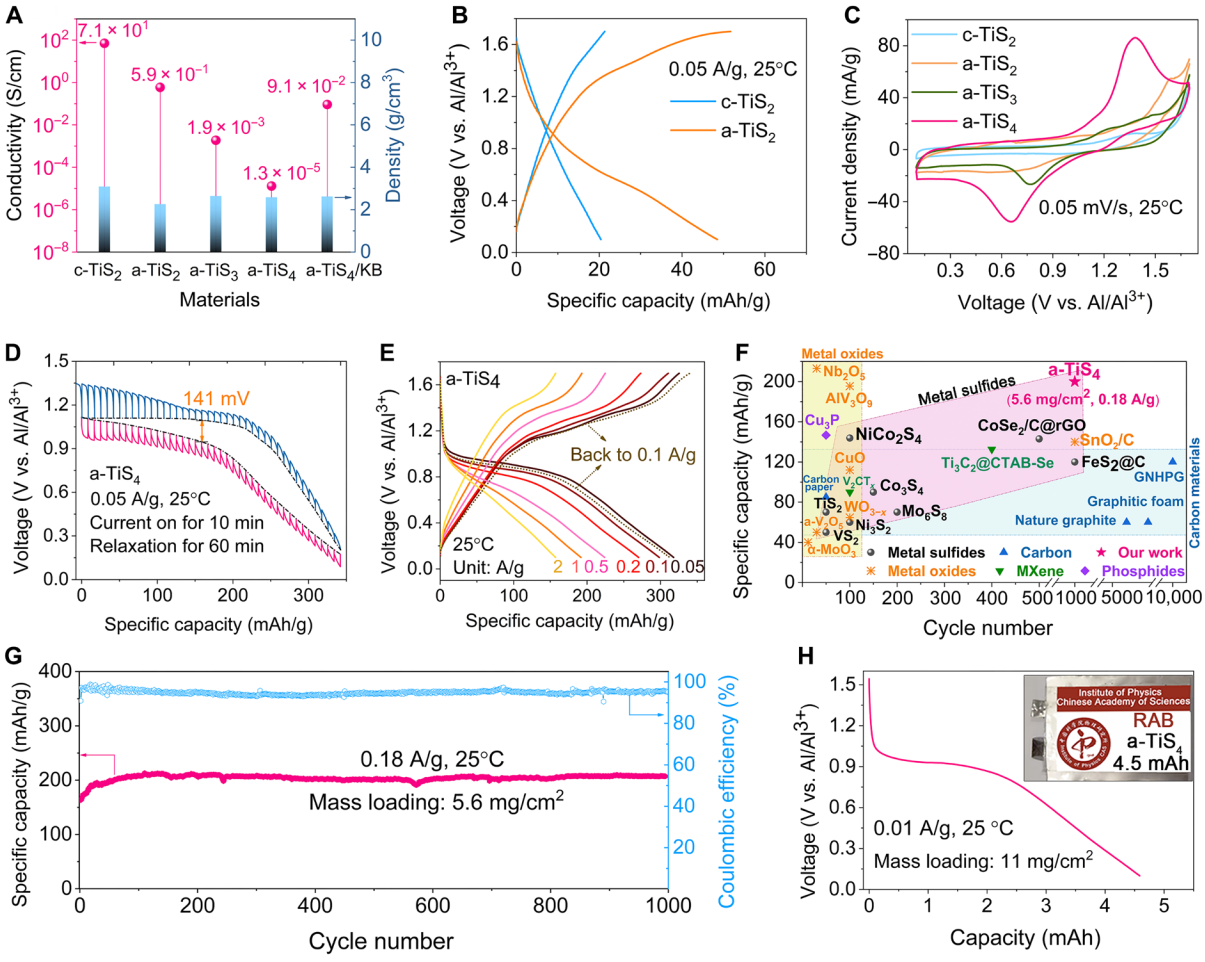


**Fig. 3. Electrochemical performance of AATPs in RABs.** (**A**) Electrical conductivity and density of AATPs. (**B**) Comparison of the typical discharge-charge curves of c-$TiS_2$ and a-$TiS_2$. (**C**) CV curves from 0.1 to 1.7 V at a scan rate of 0.05 mV/s. (**D**) Galvanostatic intermittent titration technique (GITT) curves of a-$TiS_4$. A current of 0.05 A/g was applied for 10 min, followed by 60-min relaxation. (**E**) Rate performance of a-$TiS_4$ from 0.05 to 2 A/g. (**F**) Comparison of a-$TiS_4$ cathode and other reported cathode materials for RABs (data were selected on the basis of the number of cycles and capacity of the last cycle displayed). (**G**) Cycling stability and corresponding Coulombic efficiency at a mass loading of 5.6 mg/cm$^2$ (based on a-$TiS_4$) and a current density of 0.18 A/g. (**H**) Typical discharge curves of a-$TiS_4$ with a capacity of 4.5 mAh (inset is the optical photograph of an a-$TiS_4$/Al pouch cell). Photo credit: Zejing Lin, Institute of Physics, Chinese Academy of Sciences.

(20 mAh/g), indicating that an amorphous structure is beneficial for $Al^{3+}$ storage (fig. S9). Similarly, a-$TiS_3$ (63 mAh/g) achieves a higher capacity than c-$TiS_3$ (46 mAh/g) (fig. S10). The cycling performance and corresponding voltage curves of crystalline and amorphous $TiS_x$ cathodes were also compared at 60°C to investigate the influence of increasing temperature on capacity and kinetics (figs. S11 to S14). All AATPs present similar discharge-charge curves, with a discharge slope ranging from 1 to 0.8 V and a charge plateau from 1.1 to 1.6 V. Higher capacities and smaller polarization could be obtained at 60°C. a-$TiS_4$ exhibits the highest discharge capacity of 250 mAh/g after 10 cycles of activation and maintains stability in subsequent cycles. In contrast, the c-$TiS_2$ and sulfur mixture (1:2 molar ratio, denoted as c-$TiS_2$ + 2S; fig. S15) displays a low average discharge voltage (0.44 V) and poor reversibility, further proving the notable improvement of the amorphization and sulfur enrichment strategy.

Figure 3C compares the cyclic voltammetry (CV) curves of c-$TiS_2$ with AATPs. After amorphization, all AATPs show enhanced reduction peak current, in which the broad cathodic peaks of a-$TiS_x$ electrodes appear at around 1.0 V (versus Al/$Al^{3+}$), with the peak current gradually enhanced from a-$TiS_2$ to a-$TiS_4$. The equilibrium potentials of crystalline and amorphous $TiS_x$ cathodes were measured using the galvanostatic intermittent titration technique (GITT) to obtain an accurate electrochemical signature (Fig. 3D and fig. S16). The a-$TiS_4$ sample exhibits a high discharge capacity of 342 mAh/g with a small overpotential gap of 141 mV, much better than c-$TiS_2$ (30 mAh/g, 543 mV) and a-$TiS_2$ (59 mAh/g, 548 mV). The superior performance of a-$TiS_4$ was also observed in rate capability tests under various current densities (Fig. 3E and fig. S17). A highly reversible discharge capacity of 312 mAh/g at 0.05 A/g is obtained, maintaining above 150 mAh/g at 2 A/g. When the current density returned to 0.1 A/g, the voltage platform and capacity are almost completely recovered to the values for the pristine sample, demonstrating the sustainable high current endurance of a-$TiS_4$.

To further exploit the potential of a-$TiS_4$/Al pouch cells in practical applications, the long-cycling stability was evaluated, which exhibited a capacity of 206 mAh/g after 1000 cycles with an average Coulombic efficiency of 95% under a high mass loading of 5.6 mg/cm$^2$

and a current density of 180 mA/g (Fig. 3G). The discharge-charge curves of the pouch cell virtually remain unchanged from 50 to 1000 cycles (fig. S18), indicating excellent reversibility and cycling stability. The electrochemical stability of reported representative cathode materials in RABs is summarized in Fig. 3F and table S2 to highlight the advantage of the a-$TiS_4$ sample. Here, a-$TiS_4$ cathode exhibits better long-term cycling stability than other oxides and sulfides and displays a much higher capacity than graphite materials. Furthermore, a big a-$TiS_4$/Al prototype with a high mass loading of 11 mg/$cm^2$ was constructed (Fig. 3H and fig. S19), which could deliver a high capacity of 4.5 mAh.

### Mechanism exploration upon electrochemical cycling

To explore the Al-ion storage mechanism in the amorphous sulfur-rich cathodes, a-$TiS_4$/Al batteries were dissembled at the pristine, after the first discharge, after the first charge, and after 15 cycles, as shown in Fig. 4D. During the first discharge and charge process, both Ti and S were uniformly distributed without particle agglomeration (fig. S20). The transmission electron microscopy (TEM), high-resolution TEM images, and the corresponding fast-Fourier transform patterns of the fully charged/discharged cathodes indicate no obvious ordered lattice fringes and diffraction spots (Fig. 4, A to C, and fig. S21). Combined with the XRD patterns without obvious diffraction peaks (fig. S22), it indicates that the amorphous structure is maintained throughout cycling.

Ex situ XPS S 2*p* spectra are collected to examine the chemical states of sulfur anion during the Al-ion uptake and removal process. In Fig. 4E, pristine a-$TiS_4$ shows the main doublet peaks of $S_2^{2-}$ at 162.7 and 163.9 eV. After the first full discharging, the binding energy shifts to lower energy at 161.8 and 163.0 eV, corresponding to the $S^{2-}$ peaks, demonstrating the reduction from $S_2^{2-}$ to $S^{2-}$ (*46*). When recharged, the main peaks of S 2p shifts back with the ratio of $S^{2-}$ doublet peaks decreasing notably, indicating that the $S^{2-}$ is oxidized back to $S_2^{2-}$. The intensity of the $S^{2-}$ doublet after the first charge is slightly higher than that of pristine ones, possibly due to the existence of some residual $Al^{3+}$. After the 15 cycles, the profile becomes similar to that of the pristine cathodes, confirming the high reversibility of the sulfur redox process. Electron energy loss spectroscopy (EELS) was further performed on individual particles at the S $L_{2,3}$ edge to investigate the redox process (Fig. 4F). A weak pre-edge peak is observed within 162 to 166 eV, corresponding to an interbond transition from the inner shell of S 2*p* into an

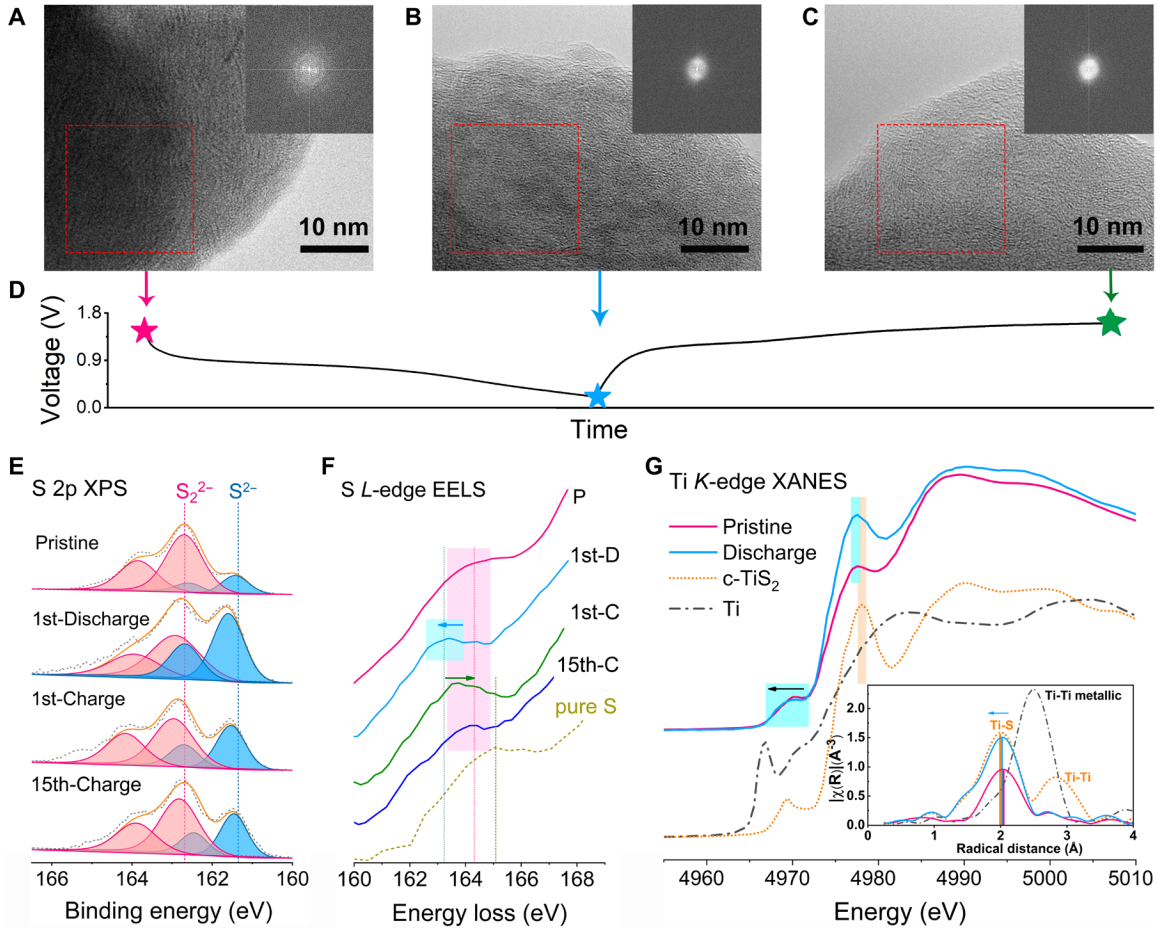


**Fig. 4. Morphology and spectral characterization to identify the redox processes.** HR-TEM images and the corresponding fast-Fourier transform (FFT) patterns (insets) of ex situ a-$TiS_4$ cathodes at (**A**) pristine, (**B**) first discharge, and (**C**) first charge states, as demonstrated in (**D**) the initial voltage profile. (**E**) XPS S 2*p* spectra and (**F**) EELS spectra at S $L_{2,3}$ edge of a-$TiS_4$ cathodes at the pristine (P), after the first discharge (1st-D), after the first charge (1st-C), and after 15 cycles (15th-C). (**G**) Evolution of Ti *K*-edge XANES spectra of a-$TiS_4$ before and after discharge compared with those of pristine c-$TiS_2$ and metallic Ti and the corresponding Fourier-transformed Ti *K*-edge EXAFS spectra (inset).

unoccupied level near $E_F$ (*27*). The element $S^0$ was used as a reference. After full discharging, the pre-edge peak shifts toward lower energy by ~1.2 eV, which is similar to the reported $S^{2-}$ state in FeS (*47*), indicating the reduction of sulfur anions when Al ions enter. At the fully charged state, the 1st and 15th pre-edge peaks are recovered at the end of the charging, further confirming the high reversibility of the sulfur redox reaction in a-$TiS_4$. No signal of the sulfur element is observed, excluding a conversion reaction.

Then, the chemical state of Ti cation in a-$TiS_4$ was analyzed by Ti 2*p* XPS spectra and Ti $L_{2,3}$-edge EELS spectra at fully discharged and charged states. There are no observable changes in the positions of the XPS Ti 2*p* peaks and Ti $L_2$ and $L_3$ peaks, revealing no obvious variance of $Ti^{4+}$ during cycling (figs. S25 and S26). To further investigate the influence of inserted $Al^{3+}$ on $Ti^{4+}$ cation, high-energy resolution Ti *K*-edge XANES spectra of the pristine and fully discharged cathodes were collected (Fig. 4G), in which the spectra of c-$TiS_2$ and Ti metal were used as references. At the fully discharged state, the Ti *K*-edge profile is similar to that of the pristine cathode without the typical signal of the pre-edge peak of Ti metal, which excluded the Ti metal as a discharge product. The main absorption edge and pre-edge peak move slightly toward the lower energy, indicating the slight reduction of $Ti^{4+}$ with the decrease in the coordination number. Moreover, the height of the main peak slightly increases, indicating that the local structure tends to be symmetrical. The coordination distance was further monitored via the Fourier transform of the $k^3$-weighted Ti *K*-edge extended x-ray absorption fine-structure (EXAFS) spectrum (the inset in Fig. 4G). The c-$TiS_2$ displays two strong peaks at 2.0 and 2.9 Å, which correspond to the nearest neighbor of Ti-S coordination and the second nearest neighbor of Ti-Ti coordination, respectively. After amorphization and sulfur enrichment, there is only one remarkable peak at 2.0 Å, which remains unchanged at the discharged state, indicating that the insertion of $Al^{3+}$ does not extend Ti-S bonds. Also, no large clusters referring to the second nearest-neighbor Ti-Ti pairs could be observed, signifying the microstructural stability of the amorphous cathodes.

Accordingly, the mechanism of Al-ion storage in a-$TiS_4$ can be concluded as follows

$$\text{a-}TiS_4 + xAl^{3+} + 3ne^- \leftrightarrow \text{a-}Al_xTiS_4\ (0 < x \leq 4/3)$$

During discharge, Al ions insert into amorphous $TiS_4$ to form amorphous $Al_xTiS_4$, with the sulfur anions acting as the main redox centers to reach local electroneutrality, which is reversible through the conversion between $S_2^{2-}$ and $S^{2-}$.

## Local structural evolution under various discharge states

To deeply understand the change in the local coordination environment of Ti and S in a-$TiS_4$ during the discharge process, amorphous structure models of a-$TiS_4$, a-$Al_{2/3}TiS_4$, and a-$AlTiS_4$ were established

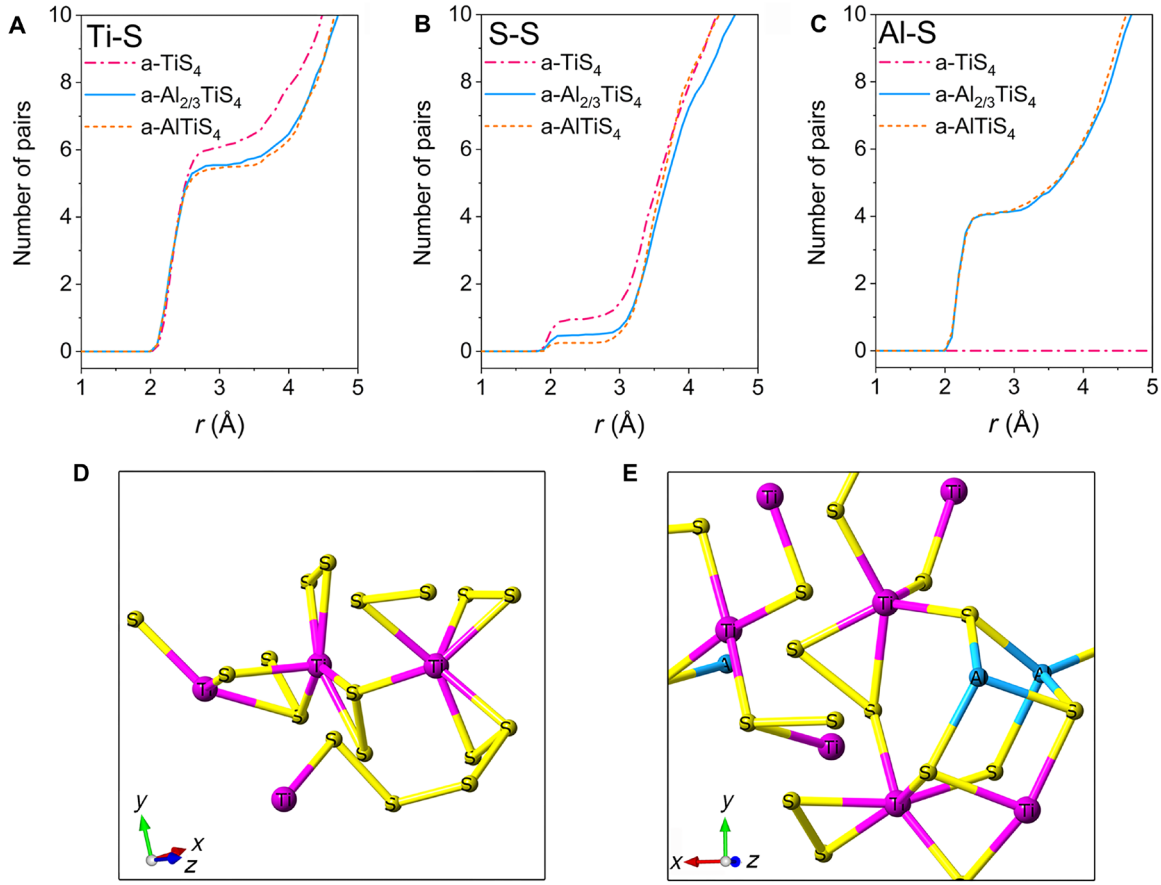


**Fig. 5. DFT-MD simulations of the local coordination environment of a-$TiS_4$ during the Al-ion insertion.** Relationship between the number of pairs and radius for (**A**) Ti-S, (**B**) S-S, and (**C**) Al-S derived from a-$TiS_4$, a-$Al_{2/3}TiS_4$, and a-$AlTiS_4$, respectively. Local structure model of (**D**) a-$TiS_4$ and (**E**) a-$AlTiS_4$.

on the basis of density functional theory–molecular dynamics (DFT-MD) simulations using a hybrid classical "melt-and-quench" approach (*30*, *48*–*50*), as shown in figs. S28 and S29. The number of nearest neighbors within a certain cutoff radius determines the coordination number. As shown in Fig. 5A, the average coordination number of Ti for the a-$TiS_4$ is about 6.6 (higher than the 6.0 of c-$TiS_2$), consistent with the Ti *K*-edge XANES results in Fig. 2E. During the discharge process, the average coordination number of Ti is reduced to 5.8 when 2/3 $Al^{3+}$ participates, and it further decreases with more Al entering. A similar trend is also observed in the average coordination number of S-S (Fig. 5B), where the calculated values are 1.2, 0.6, and 0.3 for a-$TiS_4$, a-$Al_{2/3}TiS_4$, and a-$AlTiS_4$, respectively, corresponding to the gradual dissociation of S-S bonds. With continuous discharging, the number of S-Al pairs increases notably illustrating the interaction between Al and S (fig. S30). According to the simulation, the average coordination number of S around Al was 4.1 (Fig. 5C). Thus, local structure evolution of a-$TiS_4$ before and after Al insertion is obtained: When $Al^{3+}$ enters, it interacts with sulfur anion, resulting in the reduction and dissociation of original S-S bonds, thus decreasing the Ti coordination number (Fig. 5. D and E).

## DISCUSSION

Targeting the low capacity and poor reversibility of current crystalline cathodes in multivalent metal-ion storage, we introduced a new strategy of amorphization and anion enrichment, which can not only enhance the storage sites and solid-state ion diffusion by the merits of the amorphous structure but also enhance the local transfer of multiple electrons by introducing additional anionic redox centers. We implemented the concepts by investigating a series of amorphous sulfur-rich a-$TiS_x$ in RABs. Among them, a-$TiS_4$ exhibited superior electrochemical performance regarding reversible capacity, cycling stability, and rate performance. Combining the experimental analysis of the structure and chemical states with DFT-MD simulations on local coordination environment, we confirmed that the Al-ion storage in a-$TiS_4$ cathode undergoes the reversible anion redox between $S_2^{2-}$ and $S^{2-}$, the decrease of Ti coordination number, the dissociation of S-S bonds, and the formation of Al-S bonds. Meanwhile, the amorphous structure is maintained during cycles. Overall, our investigation highlights the amorphous and anion-rich design for high-charge-density $Al^{3+}$ storage and will open up a promising avenue for developing high-energy density multivalent metal-ion batteries.

## MATERIALS AND METHODS

### Materials

The amorphous $TiS_x$ ($x$ = 2, 3, and 4) materials were prepared via the high-energy ball milling method at 800 rpm for 24 hours (Fritsch PULVERISETTE 7 premium), in which the mass ratio of zirconia balls (3 mm in diameter) to the raw materials was 10:1. The c-$TiS_2$ (99.9%, Innochem) was used as the starting material to obtain a-$TiS_2$. The a-$TiS_3$ and a-$TiS_4$ were prepared by milling c-$TiS_2$ and pure S (99.5%, Alfa Aesar) with a molar ratio of 1:1 and 1:2, respectively. To prevent overheating, the parameter was set to grind for 3 min and to idle for 7 min. The total time was recorded as the reaction time. The a-$TiS_2$/KB, a-$TiS_3$/KB, and a-$TiS_4$/KB compounds were obtained by mixing the as-prepared a-$TiS_2$, a-$TiS_3$, or a-$TiS_4$ materials with 20 wt % Ketjen Black (KB, Triquo Chemical) before ball milling was continued at 800 rpm for 24 hours. The c-$TiS_2$/KB compound material was obtained by milling 80 wt % c-$TiS_2$ and 20 wt % KB at 100 rpm for 24 hours. For the control group, the c-$TiS_2$ + 2S/KB compound was obtained by mixing the c-$TiS_2$ and pure S (1:2 molar ratio) with 20 wt % KB and milling at 100 rpm for 48 hours. Crystalline $TiS_3$ was synthesized by mixing Ti (99.5%, Innochem) and S powders with a molar ratio of 1:3, sealing under vacuum, and heating to 500°C for 72 hours. The above processes were conducted in an argon atmosphere.

### Pouch cells

The cathodes were prepared by pressing a-$TiS_x$/KB, c-$TiS_2$/KB, or c-$TiS_2$ + 2S/KB, KB, carbon nanotubes (CNT, XFNANO), and poly tetra fluoroethylene (PTFE, Alfa Aesar) at a weight ratio of 80:10:5:5 onto a molybdenum mesh. The $AlCl_3$:[EMIm]Cl (1.3:1, mole ratio) electrolyte was prepared following the previously reported procedures (*51*): [EMIm]Cl (99%, Shanghai Chengjie Ionic Liquid Company) was dried in an Ar glove box at 130°C overnight before anhydrous aluminum chloride ($AlCl_3$, 99.999%, Acros) was slowly added to it while stirring. The pouch cells were assembled using an aluminum foil (100 μm) anode, a piece of glass fiber (Whatman, GF/A) separator, the as-prepared cathode, $AlCl_3$:[EMIm]Cl ionic liquid electrolyte, and an Al plastic film package. The above procedures were carried out in an Ar-filled glove box (<0.1 parts per million of water and oxygen). The amount of electrolyte added was about 70 μl/mg (based on the weight of active materials). The specific capacity is calculated on the basis of the weight of active materials (c-$TiS_2$, a-$TiS_2$, a-$TiS_3$, a-$TiS_4$, and c-$TiS_2$ + 2S).

### Electrochemistry measurements

Galvanostatic tests were conducted using a LAND-CT2001A battery test station and a Neware battery test station. The CV was measured in a CHI604E electrochemical workstation (CH Instruments Inc.). The electrical conductivity was measured via a four-pin probe (Kyowa Electronic Instruments Co. Ltd.). In accordance with MCP-PD51, a force of 18 N was applied to the probe to obtain a good contact with the powders.

### Characterization techniques

The morphologies of samples were investigated via scanning electron microscopy (Hitachi-S4800) and TEM (JEM 2100Plus, JEOL Limited Corporation) analyses. The nitrogen adsorption-desorption isotherms of the materials were measured using TriStar II 3020 and calculated on the basis of Brunauer-Emmet-Teller (BET) analysis. The XRD (Bruker, D8-Advance x-ray diffractometer, Cu K$\alpha$, $\lambda$ = 0.15406 nm) patterns were measured from 10° to 80° (2$\theta$). TG and DSC curves were obtained (NETZSCH, STA 449C) at a heating rate of 10°C/min from 30° to 600°C in an Ar atmosphere. Raman spectra were collected at room temperature using the HORIBA Scientific LabRAM HR Evolution instrument, while the XPS was collected using a Thermo Fisher Scientific, ESCALAB 250 Xi. All samples were transferred under the protection of Ar. The binding energy scale was calibrated using the C 1s peak at 284.8 eV. The Ti *K*-edge XANES measurements were performed at beamline 14W at the Shanghai Synchrotron Radiation Facility. The incident x-ray was monochromatized using a Si (111) crystal, with the incident photon energy ranging from 4.5 to 18 keV and a beam size of about 300 μm by 300 μm. The XANES data were collected in transmission mode at room temperature, and the incident photon energy was calibrated

using a Ti foil reference sample for Ti *K*-edge XANES. All samples were well sealed in water and air-resistant polymer films to avoid contact with moist air. The EELS was conducted using an aberration-corrected scanning transmission electron microscope (STEM; JEM ARM200CF) equipped with a cold field emission gun. All tested electrodes were disassembled, rinsed with acetonitrile (99.9%, ultradry), and dried in an Ar-filled glove box before characterization.

### DFT-MD simulations

Ab initio MD simulation was performed using the CP2K code (*48*) under an constant-temperature, constant-volume (NVT) ensemble. The DZVP-MOLOPT-SR-GTH basis set was used (*49*) accompanied by Goedecker-Teter-Hutter pseudopotentials (*50*). The complementary plane-wave basis set had a cutoff of 700 Rydberg. The exchange-correlation functional used was generalized gradient approximation - Perdew-Burke-Ernzerhof (GGA-PBE). The "melt-and-quench" approach was used based on a similar reported approach (*30*). The amorphous $TiS_4$, $Al_{2/3}TiS_4$, and $AlTiS_4$, with 40, 34, and 36 atoms, respectively, were equilibrated at 2000 K for 7000 steps. Then, the temperature was slowly decreased to 300 K for 7000 steps. The cell size with the minimum energy was determined. Next, the "melt-and-quench" approach was repeated for 2 × 2 × 2 supercells for amorphous $TiS_4$, $Al_{2/3}TiS_4$, and $AlTiS_4$, with 40, 34, and 36 atoms, respectively. A time step of 1.2 fs was used for all MD simulations.

## SUPPLEMENTARY MATERIALS

Supplementary material for this article is available at http://advances.sciencemag.org/cgi/content/full/7/35/eabg6314/DC1

## REFERENCES AND NOTES


1. M. C. Lin, M. Gong, B. Lu, Y. Wu, D. Y. Wang, M. Guan, M. Angell, C. Chen, J. Yang, B. J. Hwang, H. Dai, An ultrafast rechargeable aluminium-ion battery. *Nature* **520**, 325–328 (2015).
2. H. Yang, H. Li, J. Li, Z. Sun, K. He, H. M. Cheng, F. Li, The rechargeable aluminum battery: Opportunities and challenges. *Angew. Chem. Int. Ed.* **58**, 11978–11996 (2019).
3. K. Zhang, K. O. Kirlikovali, J. M. Suh, J.-W. Choi, H. W. Jang, R. S. Varma, O. K. Farha, M. Shokouhimehr, Recent advances in rechargeable aluminum-ion batteries and considerations for their future progress. *ACS Appl. Energy Mater.* **3**, 6019–6035 (2020).
4. L. Geng, G. Lv, X. Xing, J. Guo, Reversible electrochemical intercalation of aluminum in $Mo_6S_8$. *Chem. Mater.* **27**, 4926–4929 (2015).
5. C. Wu, S. Gu, Q. Zhang, Y. Bai, M. Li, Y. Yuan, H. Wang, X. Liu, Y. Yuan, N. Zhu, F. Wu, H. Li, L. Gu, J. Lu, Electrochemically activated spinel manganese oxide for rechargeable aqueous aluminum battery. *Nat. Commun.* **10**, 73 (2019).
6. A. Zhou, L. Jiang, J. Yue, Y. Tong, Q. Zhang, Z. Lin, B. Liu, C. Wu, L. Suo, Y.-S. Hu, H. Li, L. Chen, Water-in-salt electrolyte promotes high-capacity $FeFe(CN)_6$ cathode for aqueous Al-ion battery. *ACS Appl. Mater. Interfaces* **11**, 41356–41362 (2019).
7. L. Geng, J. P. Scheifers, C. Fu, J. Zhang, B. P. T. Fokwa, J. Guo, Titanium sulfides as intercalation-type cathode materials for rechargeable aluminum batteries. *ACS Appl. Mater. Interfaces* **9**, 21251–21257 (2017).
8. Z. Li, B. Niu, J. Liu, J. Li, F. Kang, Rechargeable aluminum-ion battery based on $MoS_2$ microsphere cathode. *ACS Appl. Mater. Interfaces* **10**, 9451–9459 (2018).
9. F. Nacimiento, M. Cabello, R. Alcántara, C. Pérez-Vicente, P. Lavela, J. L. Tirado, Exploring an aluminum ion battery based on molybdite as working electrode and ionic liquid as electrolyte. *J. Electrochem. Soc.* **165**, A2994–A2999 (2018).
10. F. Wu, H. Yang, Y. Bai, C. Wu, Paving the path toward reliable cathode materials for aluminum-ion batteries. *Adv. Mater.* **31**, e1806510 (2019).
11. L. Croguennec, M. R. Palacin, Recent achievements on inorganic electrode materials for lithium-ion batteries. *J. Am. Chem. Soc.* **137**, 3140–3156 (2015).
12. T. Mori, Y. Orikasa, K. Nakanishi, C. Kezheng, M. Hattori, T. Ohta, Y. Uchimoto, Discharge/charge reaction mechanisms of FeS2 cathode material for aluminum rechargeable batteries at 55°C. *J. Power Sources* **313**, 9–14 (2016).
13. M. Liu, A. Jain, Z. Rong, X. Qu, P. Canepa, R. Malik, G. Ceder, K. A. Persson, Evaluation of sulfur spinel compounds for multivalent battery cathode applications. *Energ. Environ. Sci.* **9**, 3201–3209 (2016).
14. B. Lee, H. R. Lee, T. Yim, J. H. Kim, J. G. Lee, K. Y. Chung, B. W. Cho, S. H. Oh, Investigation on the structural evolutions during the insertion of aluminum ions into $Mo_6S_8$ Chevrel phase. *J. Electrochem. Soc.* **163**, A1070–A1076 (2016).
15. C. Legein, B. J. Morgan, F. Fayon, T. Koketsu, J. Ma, M. Body, V. Sarou-Kanian, X. K. Wei, M. Heggen, O. J. Borkiewicz, P. Strasser, D. Dambournet, Atomic insights into aluminium-ion insertion in defective anatase for batteries. *Angew. Chem. Int. Ed.* **59**, 19247–19253 (2020).
16. Z. H. Stachurski, On structure and properties of amorphous materials. *Materials* **4**, 1564–1598 (2011).
17. H. Ye, L. Ma, Y. Zhou, L. Wang, N. Han, F. Zhao, J. Deng, T. Wu, Y. Li, J. Lu, Amorphous $MoS_3$ as the sulfur-equivalent cathode material for room-temperature Li–S and Na–S batteries. *Proc. Natl. Acad. Sci. U.S.A.* **114**, 13091–13096 (2017).
18. Q. Li, Y. Xu, S. Zheng, X. Guo, H. Xue, H. Pang, Recent progress in some amorphous materials for supercapacitors. *Small* **14**, 1800426 (2018).
19. C. G. Morales-Guio, X. Hu, Amorphous molybdenum sulfides as hydrogen evolution catalysts. *Acc. Chem. Res.* **47**, 2671–2681 (2014).
20. S. B. Artemkina, A. N. Enyashin, A. A. Poltarak, A. D. Fedorenko, A. A. Makarova, P. A. Poltarak, E. J. Shin, S. J. Hwang, S. J. Kim, E. D. Grayfer, V. E. Fedorov, Revealing the flexible 1D primary and globular secondary structures of sulfur-rich amorphous transition metal polysulfides. *ChemNanoMat* **5**, 1488–1497 (2019).
21. J. R. Dahn, T. Zheng, Y. H. Liu, J. S. Xue, Mechanisms for lithium insertion in carbonaceous materials. *Science* **270**, 590–593 (1995).
22. S. Komaba, W. Murata, T. Ishikawa, N. Yabuuchi, T. Ozeki, T. Nakayama, A. Ogata, K. Gotoh, K. Fujiwara, Electrochemical Na insertion and solid electrolyte interphase for hard-carbon electrodes and application to Na-ion batteries. *Adv. Funct. Mater.* **21**, 3859–3867 (2011).
23. Z. X. Wei, D. X. Wang, X. Yang, C. Z. Wang, G. Chen, F. Du, From crystalline to amorphous: An effective avenue to engineer high-performance electrode materials for sodium-ion batteries. *Adv. Mater. Interfaces* **5**, 1800639 (2018).
24. H. Huang, X. Wang, E. Tervoort, G. Zeng, T. Liu, X. Chen, A. Sologubenko, M. Niederberger, Nano-sized structurally disordered metal oxide composite aerogels as high-power anodes in hybrid supercapacitors. *ACS Nano* **12**, 2753–2763 (2018).
25. J. B. Lee, O. B. Chae, S. Chae, J. H. Ryu, S. M. Oh, Amorphous vanadium titanates as a negative electrode for lithium-ion batteries. *J. Electrochem. Sci. Technol* **7**, 306–315 (2016).
26. G. Assat, J.-M. Tarascon, Fundamental understanding and practical challenges of anionic redox activity in Li-ion batteries. *Nat. Energy* **3**, 373–386 (2018).
27. S. Saha, G. Assat, M. T. Sougrati, D. Foix, H. Li, J. Vergnet, S. Turi, Y. Ha, W. Yang, J. Cabana, G. Rousse, A. M. Abakumov, J.-M. Tarascon, Exploring the bottlenecks of anionic redox in Li-rich layered sulfides. *Nat. Energy* **4**, 977–987 (2019).
28. Z. Li, B. P. Vinayan, P. Jankowski, C. Njel, A. Roy, T. Vegge, J. Maibach, J. M. G. Lastra, M. Fichtner, Z. Zhao-Karger, Multi-electron reactions enabled by anion-based redox chemistry for high-energy multivalent rechargeable batteries. *Angew. Chem. Int. Ed.* **59**, 11483–11490 (2020).
29. P. Afanasiev, I. Bezverkhy, Synthesis of $MoS_x$ ($5 > x > 6$) amorphous sulfides and their use for preparation of $MoS_2$ monodispersed microspheres. *Chem. Mater.* **14**, 2826–2830 (2002).
30. A. Sakuda, K. Ohara, K. Fukuda, K. Nakanishi, T. Kawaguchi, H. Arai, Y. Uchimoto, T. Ohta, E. Matsubara, Z. Ogumi, T. Okumura, H. Kobayashi, H. Kageyama, M. Shikano, H. Sakaebe, T. Takeuchi, Amorphous metal polysulfides: Electrode materials with unique insertion/extraction reactions. *J. Am. Chem. Soc.* **139**, 8796–8799 (2017).
31. A. Sakuda, N. Taguchi, T. Takeuchi, H. Kobayashi, H. Sakaebe, K. Tatsumi, Z. Ogumi, Amorphous niobium sulfides as novel positive-electrode materials. *ECS Electrochem. Lett.* **3**, A79–A81 (2014).
32. M. S. Whittingham, Lithium incorporation in crystalline and amorphous chalcogenides: Thermodynamics, mechanism and structure. *J. Electroanal. Chem. Interfacial Electrochem.* **118**, 229–239 (1981).
33. H. L. Ye, L. Wang, S. Deng, X. Q. Zeng, K. Q. Nie, P. N. Duchesne, B. Wang, S. Liu, J. H. Zhou, F. P. Zhao, N. Han, P. Zhang, J. Zhong, X. H. Sun, Y. Y. Li, Y. G. Li, J. Lu, Amorphous $MoS_3$ infiltrated with carbon nanotubes as an advanced anode material of sodium-ion batteries with large gravimetric, areal, and volumetric capacities. *Adv. Energy Mater.* **7**, 1601602 (2017).
34. Z. Rong, R. Malik, P. Canepa, G. Sai Gautam, M. Liu, A. Jain, K. Persson, G. Ceder, Materials design rules for multivalent ion mobility in intercalation structures. *Chem. Mater.* **27**, 6016–6021 (2015).
35. M. Liu, Z. Rong, R. Malik, P. Canepa, A. Jain, G. Ceder, K. A. Persson, Spinel compounds as multivalent battery cathodes: A systematic evaluation based on ab initio calculations. *Energ. Environ. Sci.* **8**, 964–974 (2015).
36. M. Sopicka-Lizer, Mechanism and kinetics of mechanochemical processes, in *High-Energy Ball Milling: Mechanochemical Processing of Nanopowders* (Woodhead Publishing, ed. 2, 2010), pp. 9–43.
37. C. Suryanarayana, Mechanical alloying and milling. *Prog. Mater. Sci.* **46**, 1–184 (2001).

38. P. Pazhamalai, K. Krishnamoorthy, S. Sahoo, V. K. Mariappan, S.-J. Kim, Supercapacitive properties of amorphous $MoS_3$ and crystalline $MoS_2$ nanosheets in an organic electrolyte. *Inorg. Chem. Front.* **6**, 2387–2395 (2019).
39. T. Weber, J. C. Muijsers, J. W. Niemantsverdriet, Structure of amorphous MoS3. *J. Phys. Chem.* **99**, 9194–9200 (1995).
40. H. Martinez, A. Benayad, D. Gonbeau, P. Vinatier, B. Pecquenard, A. Levasseur, Influence of the cation nature of high sulfur content oxysulfide thin films $MO_yS_z$ (M=W, Ti) studied by XPS. *Appl. Surf. Sci.* **236**, 377–386 (2004).
41. R. S. c. Smart, W. M. Skinner, A. R. Gerson, XPS of sulphide mineral surfaces: Metal-deficient, polysulphides, defects and elemental sulphur. *Surf. Interface Anal.* **28**, 101–105 (1999).
42. M. E. Fleet, S. L. Harmer, X. Liu, H. W. Nesbitt, Polarized x-ray absorption spectroscopy and XPS of $TiS_3$: S K- and Ti L-edge XANES and S and Ti 2p XPS. *Surf. Sci.* **584**, 133–145 (2005).
43. L. Zhang, D. Sun, J. Kang, H. T. Wang, S. H. Hsieh, W. F. Pong, H. A. Bechtel, J. Feng, L. W. Wang, E. J. Cairns, J. Guo, Tracking the chemical and structural evolution of the $TiS_2$ electrode in the lithium-ion cell using operando x-ray absorption spectroscopy. *Nano Lett.* **18**, 4506–4515 (2018).
44. F. Farges, G. E. Brown Jr., J. J. Rehr, Coordination chemistry of Ti(IV) in silicate glasses and melts: I. XAFS study of titanium coordination in oxide model compounds. *Geochim. Cosmochim. Acta* **60**, 3023–3038 (1996).
45. F. Farges, G. E. Brown Jr., Coordination chemistry of titanium (IV) in silicate glasses and melts: IV. XANES studies of synthetic and natural volcanic glasses and tektites at ambient temperature and pressure. *Geochim. Cosmochim. Acta* **61**, 1863–1870 (1997).
46. T. Gao, X. Li, X. Wang, J. Hu, F. Han, X. Fan, L. Suo, A. J. Pearse, S. B. Lee, G. W. Rubloff, K. J. Gaskell, M. Noked, C. Wang, A rechargeable Al/S battery with an ionic-liquid electrolyte. *Angew. Chem. Int. Ed.* **55**, 9898–9901 (2016).
47. S. P. Farrell, M. E. Fleet, I. E. Stekhin, A. Kravtsova, A. V. Soldatov, X. Liu, Evolution of local electronic structure in alabandite and niningerite solid solutions [(Mn,Fe)S, (Mg,Mn)S, (Mg,Fe)S] using sulfur *K*- and *L*-edge XANES spectroscopy. *Am. Mineral.* **87**, 1321–1332 (2002).
48. J. Hutter, M. Iannuzzi, F. Schiffmann, J. VandeVondele, CP2k: Atomistic simulations of condensed matter systems. *WIREs Comput. Mol. Sci.* **4**, 15–25 (2014).
49. J. VandeVondele, J. Hutter, Gaussian basis sets for accurate calculations on molecular systems in gas and condensed phases. *J. Chem. Phys.* **127**, 114105 (2007).
50. M. Krack, Pseudopotentials for H to Kr optimized for gradient-corrected exchange-correlation functionals. *Theor. Chem. Acc.* **114**, 145–152 (2005).
51. Z. Lin, M. Mao, J. Yue, B. Liu, C. Wu, L. Suo, Y.-S. Hu, H. Li, X. Huang, L. Chen, Wearable bipolar rechargeable aluminum battery. *ACS Mater. Lett.* **2**, 808–813 (2020).
52. H. Lu, Y. Wan, T. Wang, R. Jin, P. Ding, R. Wang, Y. Wang, C. Teng, L. Li, X. Wang, D. Zhou, G. Xue, A high performance $SnO_2$/C nanocomposite cathode for aluminum-ion batteries. *J. Mater. Chem. A* **7**, 7213–7220 (2019).
53. Z. Li, J. Li, F. Kang, 3D hierarchical AlV3O9 microspheres as a cathode material for rechargeable aluminum-ion batteries. *Electrochim. Acta* **298**, 288–296 (2019).
54. X. Zhang, G. Zhang, S. Wang, S. Li, S. Jiao, Porous CuO microsphere architectures as high-performance cathode materials for aluminum-ion batteries. *J. Mater. Chem. A* **6**, 3084–3090 (2018).
55. J. Tu, H. Lei, Z. Yu, S. Jiao, Ordered $WO_{3-x}$ nanorods: Facile synthesis and their electrochemical properties for aluminum-ion batteries. *Chem. Commun.* **54**, 1343–1346 (2018).
56. M. Chiku, H. Takeda, S. Matsumura, E. Higuchi, H. Inoue, Amorphous vanadium oxide/carbon composite positive electrode for rechargeable aluminum battery. *ACS Appl. Mater. Interfaces* **7**, 24385–24389 (2015).
57. K. Zhang, T. H. Lee, J. H. Cha, H. W. Jang, J. W. Choi, M. Mahmoudi, M. Shokouhimehr, Metal-organic framework-derived metal oxide nanoparticles@reduced graphene oxide composites as cathode materials for rechargeable aluminium-ion batteries. *Sci. Rep.* **9**, 13739 (2019).
58. L. Wang, H. Lin, W. Kong, Y. Hu, R. Chen, P. Zhao, M. Shokouhimehr, X. L. Zhang, Z. Tie, Z. Jin, Controlled growth and ion intercalation mechanism of monocrystalline niobium pentoxide nanotubes for advanced rechargeable aluminum-ion batteries. *Nanoscale* **12**, 12531–12540 (2020).
59. S. Li, J. Tu, G.-H. Zhang, M. Wang, S. Jiao, $NiCo_2S_4$ nanosheet with hexagonal architectures as an advanced cathode for al-ion batteries. *J. Electrochem. Soc.* **165**, A3504–A3509 (2018).
60. T. Cai, L. Zhao, H. Hu, T. Li, X. Li, S. Guo, Y. Li, Q. Xue, W. Xing, Z. Yan, L. Wang, Stable $CoSe_2$/carbon nanodice@reduced graphene oxide composites for high-performance rechargeable aluminum-ion batteries. *Energ. Environ. Sci.* **11**, 2341–2347 (2018).
61. L. Wu, R. Sun, F. Xiong, C. Pei, K. Han, C. Peng, Y. Fan, W. Yang, Q. An, L. Mai, A rechargeable aluminum-ion battery based on a $VS_2$ nanosheet cathode. *Phys. Chem. Chem. Phys.* **20**, 22563–22568 (2018).
62. K. Zhang, T. H. Lee, J. H. Cha, H. W. Jang, M. Shokouhimehr, J.-W. Choi, Properties of $CoS_2$/CNT as a cathode material of rechargeable aluminum-ion batteries. *Electron. Mater. Lett.* **15**, 727–732 (2019).
63. H. Li, H. Yang, Z. Sun, Y. Shi, H.-M. Cheng, F. Li, A highly reversible $Co_3S_4$ microsphere cathode material for aluminum-ion batteries. *Nano Energy* **56**, 100–108 (2019).
64. Y. Hu, B. Luo, D. Ye, X. Zhu, M. Lyu, L. Wang, An innovative freeze-dried reduced graphene oxide supported $SnS_2$ cathode active material for aluminum-ion batteries. *Adv. Mater.* **29**, 1606132 (2017).
65. Z. Zhao, Z. Hu, R. Jiao, Z. Tang, P. Dong, Y. Li, S. Li, H. Li, Tailoring multi-layer architectured $FeS_2$@C hybrids for superior sodium-, potassium- and aluminum-ion storage. *Energy Storage Mater.* **22**, 228–234 (2019).
66. S. Wang, Z. Yu, J. Tu, J. Wang, D. Tian, Y. Liu, S. Jiao, A novel aluminum-ion battery: Al/$AlCl_3$-[EMIm]Cl/$Ni_3S_2$@graphene. *Adv. Energy Mater.* **6**, 1606132 (2016).
67. M. Mao, Z. Lin, Y. Tong, J. Yue, C. Zhao, J. Lu, Q. Zhang, L. Gu, L. Suo, Y.-S. Hu, H. Li, X. Huang, L. Chen, Iodine vapor transport-triggered preferential growth of chevrel $Mo_6S_8$ nanosheets for advanced multivalent batteries. *ACS Nano* **14**, 1102–1110 (2020).
68. H. Sun, W. Wang, Z. Yu, Y. Yuan, S. Wang, S. Jiao, A new aluminium-ion battery with high voltage, high safety and low cost. *Chem. Commun.* **51**, 11892–11895 (2015).
69. D. Y. Wang, C. Y. Wei, M. C. Lin, C. J. Pan, H. L. Chou, H. A. Chen, M. Gong, Y. Wu, C. Yuan, M. Angell, Y. J. Hsieh, Y. H. Chen, C. Y. Wen, C. W. Chen, B. J. Hwang, C. C. Chen, H. Dai, Advanced rechargeable aluminium ion battery with a high-quality natural graphite cathode. *Nat. Commun.* **8**, 14283 (2017).
70. X. Yu, B. Wang, D. Gong, Z. Xu, B. Lu, Graphene nanoribbons on highly porous 3D graphene for high-capacity and ultrastable Al-Ion batteries. *Adv. Mater.* **29**, 1604118 (2017).
71. A. VahidMohammadi, A. Hadjikhani, S. Shahbazmohamadi, M. Beidaghi, Two-dimensional vanadium carbide (MXene) as a high-capacity cathode material for rechargeable aluminum batteries. *ACS Nano* **11**, 11135–11144 (2017).
72. Z. Li, X. Wang, W. Zhang, S. Yang, Two-dimensional $Ti_3C_2$@CTAB-Se (MXene) composite cathode material for high-performance rechargeable aluminum batteries. *Chem. Eng. J.* **398**, 125679 (2020).
73. G. Li, J. Tu, M. Wang, S. Jiao, Cu3P as a novel cathode material for rechargeable aluminum-ion batteries. *J. Mater. Chem. A* **7**, 8368–8375 (2019).


**Acknowledgments:** We thank the beamline 14W in Shanghai Synchrotron Radiation Facility (SSRF) for XANES measurement. **Funding:** This work was supported by Shell Global Solutions International B.V. (Agreement no. PT76419) and the Center for Clean Energy. **Author contributions:** Z.L. and L.S. conceived and designed the experiments. Z.L. and M.M. conducted the experiments. C.Y. and L.H. performed the DFT-MD simulation. Y.T., Q.Z., and L.G. performed TEM and EELS measurements and analyzed the data. Q.L. and X.Y. performed the XANES measurements and analyzed the data. J.Y. performed the XPS measurements. G.Y. performed the Raman measurements. Z.L., C.Y., L.H., and L.S. made the data analysis and wrote the paper. All authors discussed the results and commented on the manuscript. **Competing interests:** The authors declare that they have no competing interests. **Data and materials availability:** All data needed to evaluate the conclusions in the paper are present in the paper and/or the Supplementary Materials.

Submitted 19 January 2021
Accepted 6 July 2021
Published 25 August 2021
10.1126/sciadv.abg6314

**Citation:** Z. Lin, M. Mao, C. Yang, Y. Tong, Q. Li, J. Yue, G. Yang, Q. Zhang, L. Hong, X. Yu, L. Gu, Y.-S. Hu, H. Li, X. Huang, L. Suo, L. Chen, Amorphous anion-rich titanium polysulfides for aluminum-ion batteries. *Sci. Adv.* **7**, eabg6314 (2021).